PHYSICS OF PLASMAS **22**, 013301 (2015)

Heat loads to divertor nearby components from secondary radiation evolved during plasma instabilities

V. Sizyuk[a] and A. Hassanein[b]
Center for Materials under Extreme Environment, School of Nuclear Engineering, Purdue University, West Lafayette, IN 47907, USA

(Received 12 October 2014; accepted 22 December 2014; published online 14 January 2015)

A fundamental issue in tokamak operation related to power exhaust during plasma instabilities is the understanding of heat and particle transport from the core plasma into the scrape-off layer and to plasma-facing materials. During abnormal and disruptive operation in tokamaks, radiation transport processes play a critical role in divertor/edge-generated plasma dynamics and are very important in determining overall lifetimes of the divertor and nearby components. This is equivalent to or greater than the effect of the direct impact of escaped core plasma on the divertor plate. We have developed and implemented comprehensive enhanced physical and numerical models in the upgraded HEIGHTS package for simulating detailed photon and particle transport in the evolved edge plasma during various instabilities. The paper describes details of a newly developed 3D Monte Carlo radiation transport model, including optimization methods of generated plasma opacities in the full range of expected photon spectra. Response of the ITER divertor's nearby surfaces due to radiation from the divertor-developed plasma was simulated by using actual full 3D reactor design and magnetic configurations. We analyzed in detail the radiation emission spectra and compared the emission of both carbon and tungsten as divertor plate materials. The integrated 3D simulation predicted unexpectedly high damage risk to the open stainless steel legs of the dome structure in the current ITER design from the intense radiation during a disruption on the tungsten divertor plate. © *2015 AIP Publishing LLC*. [http://dx.doi.org/10.1063/1.4905632]

I. INTRODUCTION

Current interest in the nature of tokamak edge plasma transport and evolution is focused on several areas, including anisotropic transport properties, recycling effects, plasma temperature, surface heat loads, and component lifetimes. Edge plasma performance plays a major role in plasma confinement and controls high-confinement-mode (H-mode) operation. The edge plasma is commonly defined as the region outside the last closed flux surface (LCFS) and is characterized as an area with critical gradients in plasma parameters across the flux surfaces with significant variations along them. Most contaminated edge plasma is located in the divertor space (and is therefore called divertor plasma) and is a potential source of heavy-ion impurity in the entire scrape-off layer (SOL). Modern divertor and limiter designs in large tokamaks allow sufficient plasma purity for a sustained thermonuclear reaction. Because of the higher heat load and the potential for erosion in the surfaces in ITER and future DEMO operation, we expect that the divertor and edge plasma parameters will deviate even more from initial core plasma conditions than they do in current devices. Tokamak experiments show the multi-process complexity of the divertor/edge plasma interaction with plasma-facing components (PFCs) during instabilities and as a result, the need to understand the integrated self-consistent behavior of plasma in the entire SOL. Edge plasma drift and interaction with PFCs cause redistribution of D-T plasma and impurities from component material, changes in toroidal plasma motion, and redistribution of energy loads. Edge plasma plays an essential role in the success of fusion devices by establishing the required boundary condition for the core plasma. Plasma instabilities occur in various forms such as hard disruptions, which include both thermal and current quench, edge-localized modes (ELMs), runaway electrons, and vertical displacement events (VDEs). The associated heating and erosion of wall materials generate impurities that can migrate into the core plasma (reducing fusion gain) and affect subsequent operation. In addition, if the radiation and particle fluxes to PFC surfaces are substantially greater than expected and at unanticipated locations, the operational lifetime of the tokamak components will be severely shortened.

In most cases, theoretical studies consider these plasmas self-consistently,[1] and current existing physical models are categorized in two general groups: (a) modeling of core plasma phenomena where plasma surface interaction processes are simplified or neglected[2,3] and (b) modeling of the near-surface plasma processes (including erosion) where the core plasma parameters are assumed to be constant or predetermined.[4,5] Both approaches can be used for modeling either stable or transient tokamak operations. The first approach assumes that the core consists only of fuel D/T plasma and adequately describes core plasma dynamics and major instability parameters. However, it cannot predict directly or indirectly the influence of the component boundaries on the dynamics of the evolving divertor plasma. The second approach, opposite to the first, assumes that the developed

---

[a] E-mail: vsizyuk@purdue.edu

[b] E-mail: hassanein@purdue.edu

divertor plasma material is composed of PFCs (mainly divertor materials) and adequately predicts component surface erosion, heat loads, shielding effects, and the correct radiation transport (RT) description in the divertor plasma. The core plasma is typically described in such models as theoretically predicted or experimentally measured fuel D/T plasma flux in localized tokamak areas.[6] In general, this second approach is acceptable for divertor/edge plasma modeling. However, SOL physics includes phenomena that have bifurcation or self-consistent character; examples are Improved Divertor Confinement (IDC),[7] L-H transition effects,[8] and escaping core particle balance between low- and high-field side divertor plates.[9] In this case, the divertor and core plasmas should be considered self-consistently. A simple estimation from the energy deposited onto divertor surface during core plasma instabilities predicts a massive flow of divertor material with density up to $\sim 10^{17}\,\mathrm{cm}^{-3}$ near surface that is much higher than the SOL hydrogen plasma values $\sim 10^{13}\,\mathrm{cm}^{-3}$. These conditions allow treating the divertor plasma evolution as the main process and the core/SOL plasma processes as perturbations to the main process by modeling of the nearby surface phenomena. This dense divertor plasma hydrodynamic evolution enables the use of the extensive models developed for laboratory plasma devices. The magnetohydrodynamics (MHD), atomic physics, radiation transport, and heat conduction processes can be simulated in the dense evolving divertor plasma similarly to laser- or discharge-produced plasma devices.[10]

Based on our previous results,[6,11] we should emphasize that the PFC heat load processes, erosion dynamics, and damage spatial profile are closely intercorrelated with the escaped core plasma parameters, divertor MHD evolution, and radiation transport processes during ELMs and disruptions. To simulate realistic tokamak divertor/edge/core plasma interdependences, we have developed, implemented, and benchmarked new kinetic Monte Carlo models for the escape of core plasma particles during these events.[9] The main goal of that study was to integrate Monte Carlo models of core plasma impact with a MHD description of the evolving contaminant plasma into one hybrid model and simulation package in the upgraded HEIGHTS package. Surface vaporization due to intense power deposition is the main mechanism of divertor plasma initiation. Macroscopic erosion and splashing of melt layers during plasma transients are treated separately.[12] This mixed approach provides the advantage (compared to most existing models) of considering properties of the core and divertor plasma in parallel. In this approach, the divertor plasma is not simple hydrogen ions but is a partially ionized contaminated plasma of the surface material as seen in various laboratory plasma applications,[10,13] specifically carbon or tungsten contaminants in the present study. The core plasma is described as clean D/T flow in a kinetic model.[9]

Radiation transport is usually considered the most important aspect when simulating laboratory plasma devices used as radiation sources. The spectral and output power characteristics of the laser- or discharge-produced plasma devices should be described very accurately, for example, in the optimization of future extreme ultraviolet (EUV) advanced lithography sources.[14] The significant progress and success achieved in the modeling and simulation of these plasma devices are now being used for tokamak divertor plasma modeling. In this paper, we present the new Monte Carlo radiation transport model developed and incorporated into our HEIGHTS computer package and show new and detailed results of PFC and nearby surface heat loads that have never been predicted before.

Detailed analysis of the radiative excitation processes is possible by combined solution of the equations of atomic-level kinetics and radiation transport in the whole plasma domain, such that the solution is self-consistent for photon transport. In such a case, the problem becomes nonlocal, and its implementation requires significant computational resources. Currently, it is a huge time-consuming to solve such equation set during every hydrodynamic time step of the plasma evolution.

The processes of radiative excitation and photoionization are neglected in the original collisional-radiative-equilibrium (CRE) model. Therefore, the CRE model satisfactorily describes the optically thin plasma. One of the methods to include self-consistency in description of the populations of atomic levels is expansion of the CRE model by including additional effects. The nature and order of the enhancement tend to be conditional and depend upon the initial state of the problem considered. The general approach is introducing such additional nonlocal effects such as decreasing the probability of spontaneous transitions (usually in the form of an escape probability approximation), including the probability of photoionization and accounting for Auger processes.

In our calculations, we consider self-consistent effects using the escape probability approximation for line transitions and direct photoionization for the continuum spectrum. The photoionization from deep inner states may also generate cascades of Auger processes. Special attention is paid to the calculation of atomic levels populations in non-steady state approximation. The main idea of the applied escape probability approximation is that nonlocal effects can be reduced to a local treatment, e.g., absorption of some of the photons is equivalent to decreasing their spontaneous emission. Therefore, for example, accounting for absorption leads to substitution of the probability of spontaneous transition Wij by the value ΘWij, where Θ is the escape factor.[15] Determination of detailed opacities was the subject of our previous analysis, and publication and the results are only referenced in this paper. Optical coefficients of candidate materials were precalculated and tabulated during our extensive investigations of discharge- and laser-produced plasma devices, such as plasma focus, z-pinches, hollow cathode devices, etc., which are appropriate to use based on the enhanced CRE model. Those studies showed good agreement of our calculations with several experiments, for example, in EUV photon generation sources.[14] Divertor-generated plasma (i.e., impurity plasma of divertor material such as tungsten or carbon) during giant ELM and disruption is sufficiently dense over a longer time scale, as predicted from the self-consistent integrated solution and energy conservations.

The plasma conditions are very similar to those in previous studies of discharge- and laser-produced plasma.

We confirm that the predicted ELM and disruption parameters for ITER will increase contamination inflow into the divertor space area.[16] In the case of a high-Z divertor plate, contamination initiates an intense radiation source in divertor space area during transient core plasma impact. We show strong dependence of the radiation fluxes and component heat loads on the choice of divertor plasma material and the potential damage of nearby surfaces as a consequence of disruptions or giant ELMs on the main divertor material.

II. MONTE CARLO PHOTON TRANSPORT MODEL

Earlier we reported that direct Gauss integration of the radiation transport equation[17]

$$\frac{1}{c}\frac{\partial I_\nu}{\partial t} + \mathbf{\Omega}\nabla I_\nu = k'_\nu (I_{\nu p} - I_\nu) \tag{1}$$

will result in a significant computation load in order to achieve reasonable accuracy.[18] Here, I_ν is the spectral intensity, $I_{\nu p}$ is the spectral equilibrium intensity, c is the speed of light, t is the time, and Kirchhoff law determines coefficient k'_ν as expressions for emission k_{em} and absorption k_{abs} coefficients

$$k_{em} = k'_\nu I_{\nu p}, \quad k'_{\nu p} = k_{abs}[1 - \exp(-\hbar\omega/T)], \tag{2}$$

where $\hbar$ is the reduced Planck's constant, ω is frequency, and T is plasma temperature. Similarly, direct Monte Carlo simulation methods of the entire ensemble of radiation particles require large memory to track various particles parameters.[19] We developed weighted Monte Carlo methods for detailed calculations of photon emission, propagation through the SOL, and deposition into the wall/evolving vapor plasma and into nearby components. The algorithm is based on data analysis and statistics regarding the generation and subsequent evolution of particles using precalculated optical coefficients and has the advantage of being relatively straightforward in applying complex geometries such as illustrated in Fig. 1. The divertor plasma cloud has complex space structures, dynamics, and highly non-linear dependence of the optical coefficient values on the local plasma parameters. We used numerical schemes with weighted hierarchies of statistically accumulated events. Two major weight factors were implemented: normalization of emitted photon "bundles" relative to the most radiated cell in the computational domain and normalization of the photon bundle magnitudes relative to optical thickness of the cell. The first weight coefficient enables us to detail the emission processes by neglecting cold cell emission. The second coefficient allows "idle" processes to be ignored, such as those with emitting and absorption in one cell (absorbed lines). These coefficients helped significantly in decreasing the computational time.

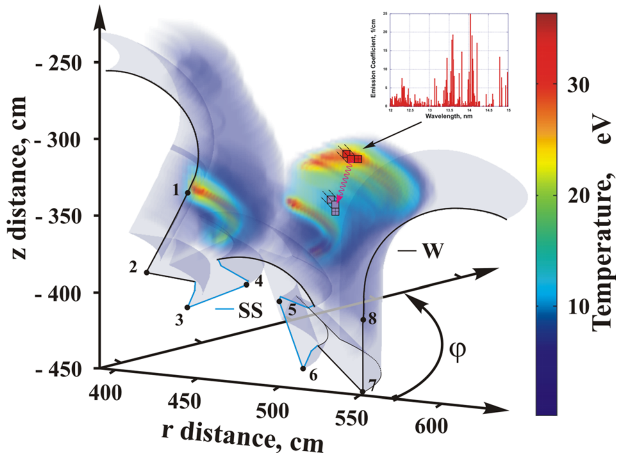

FIG. 1. Schematic illustration of Monte Carlo RT model for ITER geometry: 1–8 are dedicated points.

From the results of the preliminary calculations in strongly nonuniform mesh, a third weight coefficient was found to be useful. If the volume of the emitting cell is very small, the amount needed to simulate photon bundles should not be zero in order to prevent exclusion of extremely small cells (in the most important regions) from the radiation transport. The volume weight coefficient increases computation accuracy considerably in this case. Implementation of these three weight coefficients made our 3D Monte Carlo methods very efficient, enhanced the accuracy of the methods, and accommodated the complex 3D realistic geometry.

As previously described,[17] to obtain the number N of photons emitted in space (per unit volume per unit time), the emission coefficient k_{em} should be integrated with Planck's function $B(\omega)$ in the full spectrum

$$N = 4\pi \int_0^\infty \frac{k_{em} B(\omega)}{\hbar\omega} d\omega, \quad \text{where } B(\omega) = \frac{\hbar\omega^3}{4\pi^3 c^2}\left(e^{\frac{\hbar\omega}{T}} - 1\right)^{-1}. \tag{3}$$

For convenience in the optical parameters calculations, we use the Gaussian unit system with the energy and temperature units given in electron volts [eV]. Integration of the number of photons gives the following expression that we used in our numerical simulations:

$$N = \int_{E_{\min}}^{E_{\max}} \frac{k_{em}(E, T, \rho) E^2}{\hbar^3 \pi^2 c^2}\left(e^{\frac{E}{T}} - 1\right)^{-1} dE, \tag{4}$$

where E is energy of emitted photon; $E_{\min}, E_{\max}$ is the spectral energy range; $k_{em}(E, T, \rho)$ is the emission coefficient; and ρ is the plasma density. From the adaptive mesh refinement (AMR) cell volume V_i, temperature T_i, and density ρ_i, we calculate the total amount of photons N_i generated per unit time:

$$N_i = V_i \int_{E_{\min}}^{E_{\max}} \frac{k_{em}(E, T_i, \rho_i) E^2}{\hbar^3 \pi^2 c^2}\left(e^{\frac{E}{T_i}} - 1\right)^{-1} dE, \tag{5}$$

where i is the cell index in unstructured mesh. By analogy with the emission process, attenuation of light intensity as a result of absorption in mixed media can be expressed as $I = I_0 \exp\{-\int_0^l k_{abs}(\omega, l)\, dl\}$ or in photon-number terms[20]

$$N(\omega) = N_0(\omega)\exp\left\{-\int_0^l k_{abs}(\omega,l)\,dl\right\}. \tag{6}$$

Here, $N_0(\omega)$ is the initial number of photons with frequency ω, and l is the path length. Considering the photon path within one cell (where we assumed that the absorption coefficient does not change inside the cell space) attenuation can be expressed as

$$N(\omega) = N_0(\omega)\,\exp\{-k_{abs}(\omega)l\}. \tag{7}$$

The absorption P_{abs} and transition P_{trans} probabilities of the photon along the path with length l in the $\{i\}$ cell following Eq. (6) are given by

$$\begin{aligned} P_i^{abs}(\omega) &= 1 - \frac{N(\omega)}{N_0(\omega)} = 1 - \exp\left\{-k_{abs\{i\}}(\omega)\,l\right\}, \\ P_i^{trans}(\omega) &= \exp\left\{-k_{abs\{i\}}(\omega)\,l\right\}. \end{aligned} \tag{8}$$

After the sampling of photon energy, photon transport in computational domain cells is simulated by checking each cell for absorption probability. The sum of all sampled emission and absorption results, i.e., $N = \sum_i N_i^{sim}$, gives information about energy redistribution in the computational domain due to photon transport. The total number of photons in the most radiated cell is used for the initial normalization of the photon bundles. A reasonable degree of accuracy requires that the minimum simulation number of emission be not less than N_{sim}. Based on this assumption, the first weight coefficient of photon bundle can be written as

$$W_1 = \frac{N^{\max}}{N_{sim}}, \tag{9}$$

where $N^{\max}$ is the integral (Eq. (5)) in the most radiated cell and N_{sim} is the real number of photons that will be sampled in this largest cell. To obtain reasonable accuracy for the radiation transport calculations, we require generating $N_{sim} \sim 10^3$ photons in most radiated cells. With the Monte Carlo radiation transport method, one can simulate situations in which a spectral band can be completely absorbed within one cell volume. Our Monte Carlo algorithm in this case defines an "idle case," i.e., particle energy is subtracted from cell energy by emission simulation and is added by absorption in the same cell. The second weight coefficient introduced to solve this problem is given by

$$W_{2\{i\}}^n = k_{abs}(E_n, T_i, \rho_i)\,\Delta r_i, \tag{10}$$

where $W_{2\{i\}}^n$ is the weight coefficient of the nth spectral range in the $\{i\}$ cell; $k_{abs}(E_n, T_i, \rho_i)$ is the absorption coefficient of the nth spectral range in the cell $\{i\}$; and Δr_i is the characteristic size of the cell. If the expression (Eq. (10)) is less than 1, the second coefficient is set equal to 1. We assume that the photon energies are distributed equally within one spectral range. Hence, linear interpolation was used to sample the emitted particle energy E_{ph}. Taking into account both weight factors gives the energy of the photon bundle $E_{ph}^{sim} = E_{ph}W_1W_{2\{i\}}^n$ as a function of the spectral range number n. The range number is determined with the real physical energy of photon E_{ph}. During the RT simulation, the value E_{ph}^{sim} is subtracted from the cell energy by the emission processes and added by the absorption processes. The balance between the cell emitted and absorbed energy is the source term Q_{rad} in Eq. (1) of Ref. 9. This term determines energy redistribution in plasma due to radiation and in ideal case should be recalculated for each MHD time-step. In practice, the MHD and RT time-steps can be unequal and are determined according to the required calculation accuracy and numerical stability of the solution. Applying additional counters at the cell borders allows calculation of the radiation fluxes in matter. The model easily determines the radiation fluxes on surfaces having complex geometry. This is very important for calculating the effect of vapor radiation on nearby "hidden" components. The following algorithm is applied to calculate radiation load from the divertor plasma cloud into the tokamak surfaces. Dynamically (every hydrodynamic time step) we (1) determine number of photons that should be born in a cell; (2) randomly sample individual photons based on a local plasma opacities, i.e., determine ascribed physical sizes in eV and initial directions; (3) calculate absorption probability on the photon ways based on the local cell plasma properties; and (4) accumulate data about the emission and absorption acts. The time step recount of the surface absorbed photons gives the time dependent energy load of all tokamak components during the instabilities and disruptions.

In calculating radiation transport in plasma, the integral radiation fluxes depend to a great extent on the level of detail and the precision of the optical coefficients. In turn, the computational accuracy and completeness of the calculated opacities depend on the accuracy and completeness of the atomic data. Because the details of opacity and atomic data calculations are beyond the objectives of this paper, we refer to our previous publications.[21,22] Briefly, we note that the structure of atomic energy levels, wavefunctions, transition probabilities, ionization potentials, oscillator strengths, broadening constants, photoionization cross sections, and other atomic characteristics are calculated by using the self-consistent Hartree-Fock-Slater (HFS) method.[23] The CRE model[24] was used to calculate the populations of atomic levels and the ion and electron plasma concentrations. Because the original CRE model satisfactorily describes the optically thin plasma, the escape probability approximation for line transitions and direct photoionization for the continuum spectrum was applied to reduce the nonlocal radiation effects.[15] From our developed and implemented HFS-CRE models, the thermodynamic and opacity properties of both C and W plasmas were calculated in a wide range of densities and temperatures, i.e., from 10^{10} to $10^{21}\,\mathrm{cm}^{-3}$ and from 0.02 to 250 eV, respectively. The emission and absorption coefficients were also determined by using the CRE model in a wide range of photon energies from 5×10^{-2} to 1×10^5 eV and with super-fine mesh (10^5 points per full spectrum) for detail isolation of thin spectral lines. However, taking into account additional plasma density and temperature scales results in an enormous data array of density/temperature/photon energy $(15 \times 30 \times 10^5)$ that cannot be used in a reasonable

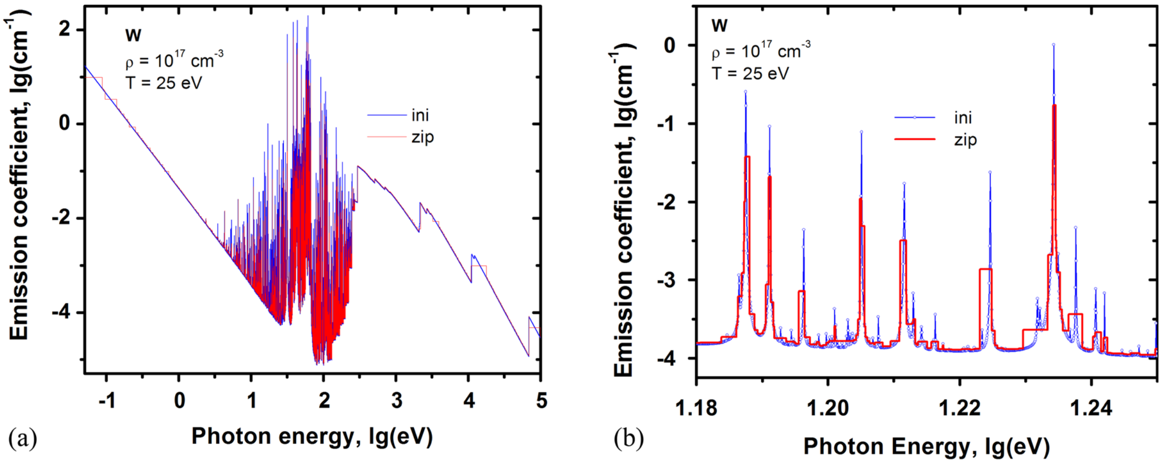

FIG. 2. Optimization of tungsten opacities of divertor plasma for RT calculations (a) full spectrum and (b) fine structure.

time for integrated 3D simulations of the entire device. On the other hand, as shown in our previous laboratory plasma studies,[10,25] correct radiation transport modeling requires a detailed consideration of energy transfer in strong lines along with the continuum spectra. To allow simulation of RT having strong lines, we optimized the initial opacity tables and separated the full plasma spectrum into spectral groups where optical coefficients are relatively invariable. Using such technique, the opacity tables were reduced by an order of magnitude for complex elements as tungsten and by two orders of magnitude for the lighter elements such as carbon and lithium. Figure 2 shows sample optimization of tungsten opacities for a preset ratio of opacity variation $R = 0.5$, where R is the variation ratio determined as the opacity change ratio inside the selected spectral group. Because the plasma spectrum depends critically on the temperature, the collected spectral groups are different for each temperature value. The specially developed computer code (i.e., Spectrum Zipper) combines group locations in one final set, which are valid for all temperature values and that recalculates the opacities for each group.

This recalculation is based on conservation of the total photon number given by Eq. 4. In that way, the variation ratio R becomes an initial variable that determines the final group's amount and the final accuracy of the RT calculations as a result. Preliminary calculations showed reasonable RT calculations accuracy with $\sim 2 \times 10^4$ groups for tungsten (19913 groups in Fig. 2), $\sim 3 \times 10^3$ groups for carbon, and $\sim 2 \times 10^3$ groups for lithium that depends evidently on the complex atomic structure of the element.[26] To validate the developed RT model and to benchmark HEIGHTS package, we simulated several laboratory plasma problems and compared our results with known analytical and experimental results. The agreement is very good, and more-detailed information about numerous validation of our new RT model can be found in Refs. 25–28.

III. SIMULATION RESULTS

We implemented the above described radiation transport model in our HEIGHTS package and integrated it with the earlier developed model of the escaping core plasma,[9] the adaptive mesh refinement magnetohydrodynamic model for the edge plasma,[9] the magnetic diffusion, and multiscale mesh coupling of subsurface processes with the SOL plasma models[6] for the detail simulation of the reradiation phenomena in edge divertor plasma. We simulated the evolution of the initiated divertor plasma and particularly its radiation characteristics during and directly after an ELM and a disruption in the ITER device with its current full 3D divertor design.[29] Using the predicted ITER core plasma parameters,[6] we calculated the radiation fluxes and heat loads on component surfaces for C and W as potential candidate divertor materials. A schematic illustration of the computational domain in the poloidal cross section is shown in Fig. 3. Initial magnetic field structure and location of various component materials are also shown. As in our previous study,[9] we

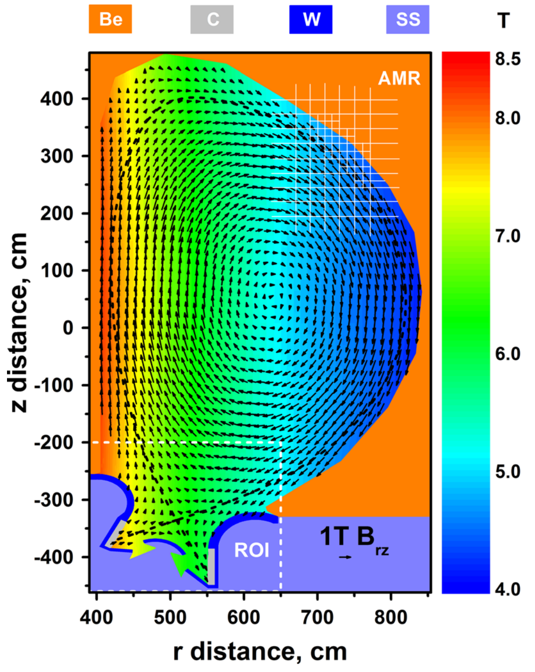

FIG. 3. Schematic illustration of computational domain with AMR and various component materials in poloidal cross section: Be (first wall), C (divertor plate), W (divertor), and SS (stainless steel elements). The tokamak major radius is taken as r-axis; the torus symmetry axis of is taken as z-axis.

started from the equilibrium magnetic field configuration extracted from the EQDSK database files and assumed the initial divertor plasma pressure of 10 Pa. Figure 3 shows carbon as the divertor plate material, but in the calculations below, we also compared tungsten and lithium under similar plasma impact conditions. Implementation of the AMR mesh allowed simulations in the entire SOL area, and the presented results are calculated self-consistently, involving all physical processes throughout the SOL. For example, see our discussion in Ref. 9 about particle balance between the low- and high-field divertor plates. Below, we present the simulation results in zoomed regions of interest (ROI); see Fig. 3 for better clarity.

From our preliminary simulation results, RT in the divertor plasma plays a key role in the heat flux load of ITER components and surface erosion.[6] We predicted the damage due to indirect radiation to the nearby components during giant ELMs and disruptions on divertor plate using local domain simulations. Our simulations show that the radiation fluxes and heat loads to nearby surfaces depend not only on the local impact parameters but also on the integrated behavior of the whole SOL plasma and how that depends on the properties and evolution of the divertor plasma material.

The divertor plasma that develops as a result of disruptions/ELMs is composed mainly of component materials which greatly increase the contribution of radiation transport in the total energy balance compared to that of clean DT plasma.[30,31] To determine the difference in performance, we compared the incident radiation flux on the divertor surface during a giant ELM for tungsten, carbon, and lithium as potential divertor materials. The giant ELM energy (10% of the total) was assumed to be $Q = 12.6\,\text{MJ}$, temperature of escaped core plasma $T = 3.5\,\text{keV}$, and the impact duration $\tau = 0.1\,\text{ms}$. A detailed description of the core-plasma-escaping model and its numerical implementation with initial and boundary conditions is presented in Ref. 9. The considerable differences in radiation flux shown in Fig. 4 for the W, C, and Li divertor plates are striking evidence of the importance of PFC material choice in tokamak design. The flux distribution is shown for the time $t = 30\,\mu\text{s}$ between locations 7 and 8 (see Fig. 1 for specific point locations). The time-moment in this figure and below is used due to the sufficiently developed physical processes and the start of intense overheating of stainless steel components during a disruption at this time.

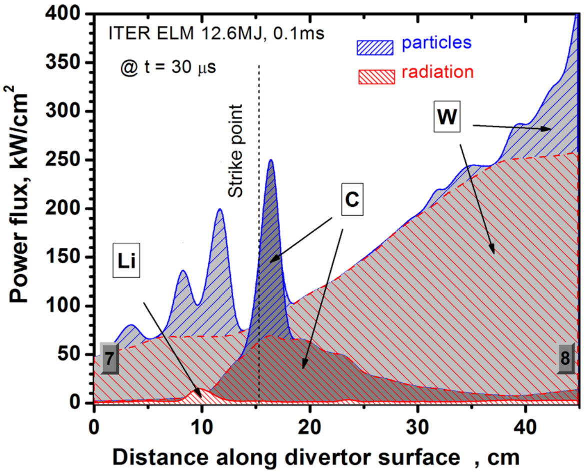

FIG. 4. HEIGHTS predicted radiation (left incline) and particle (right incline) fluxes on ITER divertor plate surface during giant ELM.

It can be seen that the radiation power from tungsten-developed plasma is very high compared to those of carbon and lithium. We did not specifically calculate the radiation flux (assuming hydrogen plasma), but it can be estimated readily as very low from Fig. 4 by extrapolation of the data shown. The calculated radiation fluxes confirm not only increased total radiation energy load from the divertor material for the higher-Z materials, but also show differing spatial divertor plasma evolution for the same incident ELM parameters. Core plasma impact energy is distributed among three different regions: direct particle energy deposition into divertor surface, developed vapor and plasma heating, and radiation of heated plasma to nearby components. Figure 4 shows that a large portion of the initial plasma impact in the case of the carbon divertor plate is spent on plasma thermal energy, i.e., the temperature of the carbon cloud would be much higher than that of the tungsten cloud.

The radiation flux peak has a certain forward shift with the material's atomic number, as shown in Fig. 4, i.e., different plasma cloud evolution, location, and plasma shielding characteristics. Different plasma dynamics have different plasma densities and temperature distributions, which determine the maximum fluxes around the radiated plasma cloud. Figure 5 shows distribution of plasma temperature where considerably lower temperatures can be seen in the developed divertor plasma in the tungsten case. According to our HEIGHTS simulation, the volume and drift velocity of the hot plasma area is also several times lower in the tungsten divertor than in the carbon case. However, this could have negative consequences for the final heat load of divertor components. As noted above and discussed in Ref. 9, the self-consistent treatment of particle drift in SOL correctly predicts the energy exchange between the low- and high-field tokamak sides (i.e., inner and outer divertor plates) and the resulting additional damage to the low-field divertor plate in the tungsten case.

Development of the second high-temperature area above the low-field divertor plate is noticeable in Fig. 5(b), left side. Individually, plasma temperature does not determine the final radiation flux profiles, but is coupled with plasma density and the input energy. Figure 4 shows that the carbon peak location of the radiation flux is closer to the strike point, while the temperature distribution indicates the opposite situation. Previously, we studied the effect of various processes on plasma evolution in future plasma lithography sources with regard to the conversion efficiency of these sources for emission and collection of EUV photon radiation power.[32] Opposite to the expectation that radiation power is determined with the correct plasma density/temperature combination,[33] we found that radiation transport and hydrodynamic processes coupled with the external input energy play critical role in determining the final emitted radiation power. The giant ELM simulations predict lower evolution of plasma density in the tungsten divertor case with a maximum of $\sim 10^{16}\text{cm}^{-3}$ at the second-highest temperature area above the

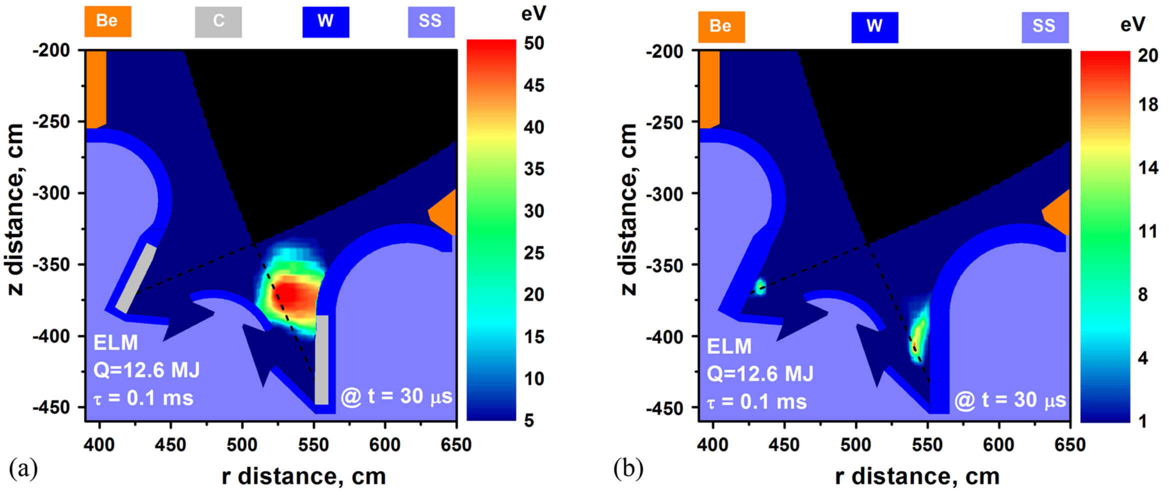

FIG. 5. Distribution of plasma temperature in divertor space during giant ELM: (a) carbon divertor plate and (b) tungsten divertor plate.

low-field plate (Fig. 6). However, as we found this level of high-Z impurities is sufficient for initiation of a high-power radiation source in the divertor space. The escaping core plasma particles are the energy source for the generation and evolution of the divertor shielding plasma and consequently determine the location and size of the developed radiation source. Most of the radiated area in the evolving plasma cloud is the result of three dynamic components: density, temperature, and input energy.

Figure 7 shows that deposition/absorption of the escaped core particles energy in the evolving divertor plasma is the main determining process of radiation emission. The produced divertor plate plasma has sufficient density in this area for effective absorption of the incident impact energy and the subsequent radiation emission from the localized hot temperature areas.

Comparison of the input energy areas, temperature distribution, and full area of the calculated radiation fluxes shown in Fig. 8 illustrates the dynamic formation of the radiated plasma cloud/blob and the shielding processes. This can be seen in the tungsten case by the much higher radiation fluxes and larger exposed areas. In our previous work,[6] we predicted the high values of radiation fluxes on the divertor's nearby surfaces, but in this work we show the effect of various divertor materials on the final thermal response of the "hidden" dome components in the current ITER design. Figure 8(b) shows that the open legs of the umbrella are the highly exposed and high-risk location for the secondary radiation heat load from the evolving tungsten divertor plasma, particularly on those cooling tubes made of stainless steel.[29]

The upgraded HEIGHTS integrated models can now calculate the direct (from the escaped core particles) and indirect (from photon radiation) heat loads and heat conduction inside all tokamak chamber surfaces due to the AMR implementation methods.

Figure 9 shows the calculated surface temperature of ITER umbrella tubes on the low-field side between locations 5 and 6 (see Fig. 1 for point locations) during the ELM and disruption. The giant ELM (Fig. 9(a)) insignificantly heats the stainless steel tubes in the case of carbon divertor plates but up to ∼900 K in the tungsten case, which may also be acceptable. The initial temperature of the tubes was assumed to be 500 K. In contrast to the ELM case, a full disruption on a

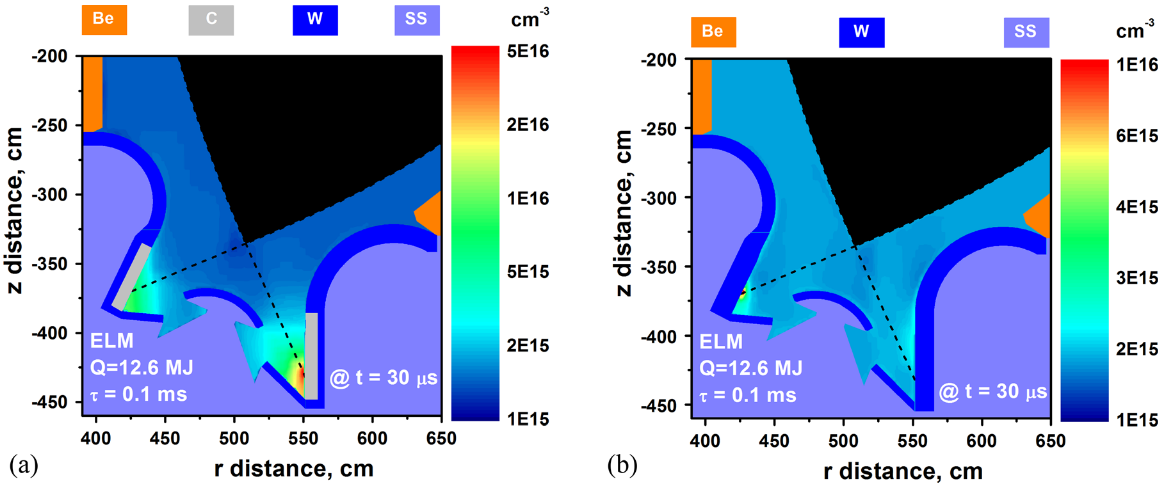

FIG. 6. Distribution of plasma density in divertor space during giant ELM: (a) carbon divertor plate and (b) tungsten divertor plate.

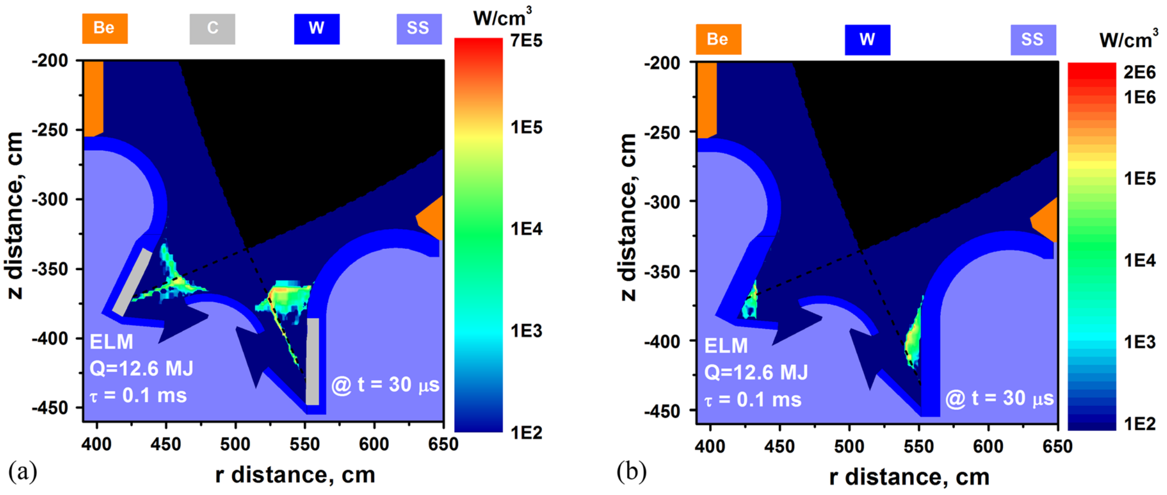

FIG. 7. Energy deposition of escaped core particles into the generated divertor plasma cloud during giant ELM in ITER: (a) carbon divertor plate and (b) tungsten divertor plate.

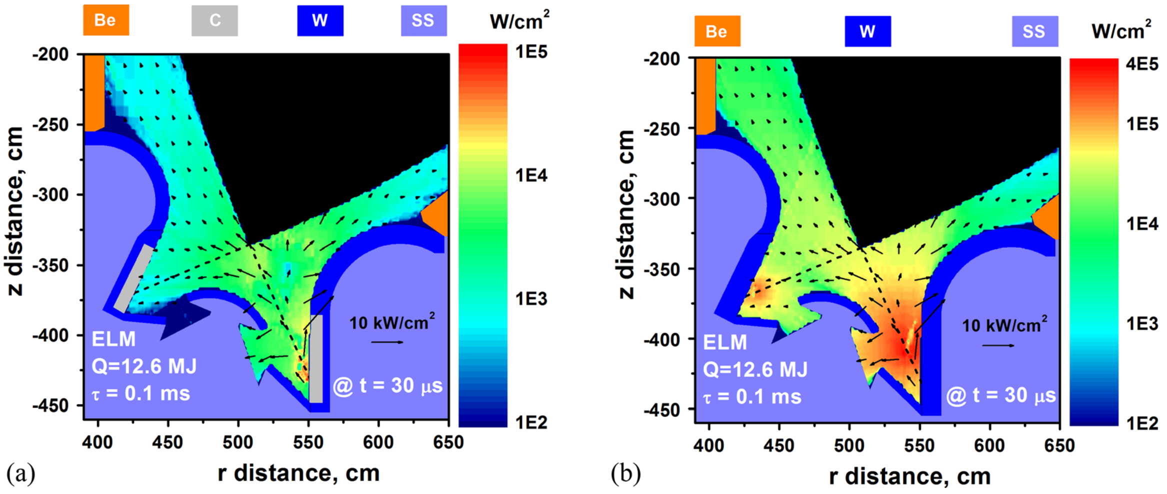

FIG. 8. Distribution of radiation fluxes in divertor space during giant ELM: (a) carbon divertor plate and (b) tungsten divertor plate.

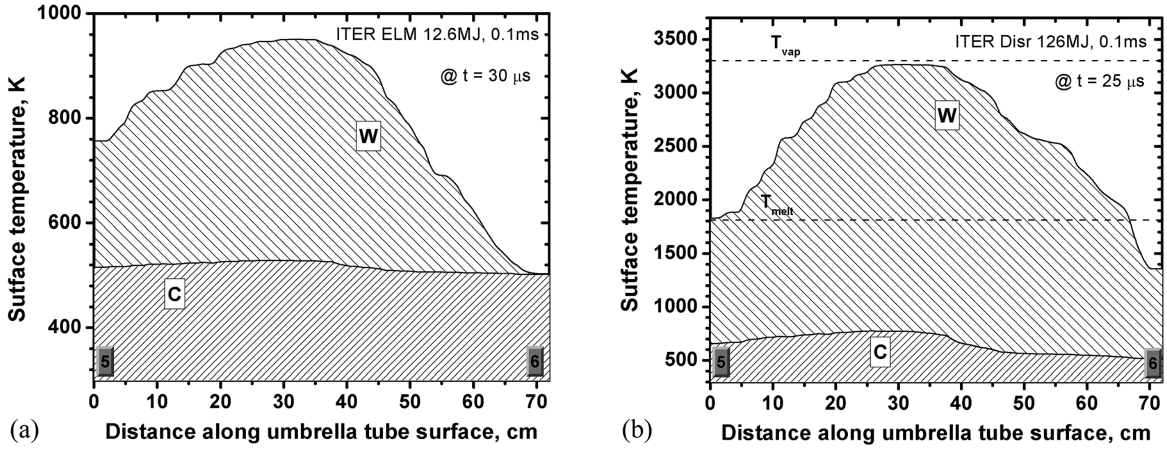

FIG. 9. Temperature distribution of dome leg surface during (a) giant ELM and (b) disruption.

tungsten divertor will cause significant heating of the tube surface and up to the melting and vaporization temperatures in the first 25 μs (Fig. 9(b)). Melting and vaporization temperatures of stainless steel are marked with dashed lines. As in our previous study,[6] we assumed the full discharge energy to be $Q_{DIS} = 126\,\text{MJ}$, disruption duration $\tau = 0.1\,\text{ms}$ and temperature of the escaped core plasma $T = 3.5\,\text{keV}$.

In the case of a carbon divertor plate, no significant overheating of the umbrella tubes is expected during disruptions. Figure 10 shows the dynamics of surface heating in the

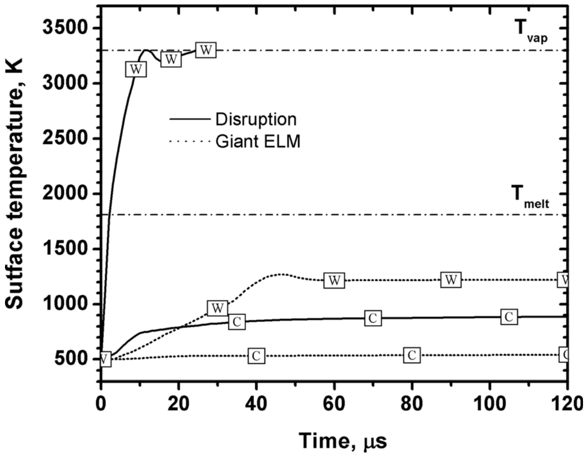

FIG. 10. Dynamics of SS tube radiation heating during ELM and disruption.

most irradiated section of the umbrella tubes placed at distance of ∼32 cm between the 5 and 6 locations (Fig. 9). The surface temperature increases up to the maximum value in the first 10 μs of the disruption, while in a giant ELM it reaches a much lower temperature peak over a longer time because of the lower radiation power. The maximum temperature and location in the tungsten case is due to the small hot size of the radiated plasma cloud relative to that of the carbon plasma. The maximum temperature corresponds to the location of the drifted divertor plasma closely to the monitored surface. The subsequent decrease in temperature is related to the umbrella shielding, which is not as effective for the initially larger carbon plasma cloud.

The relevant SOL plasma parameters summarized in Table I confirm the complex self-consistent behavior of the escaped core plasma-divertor surface interaction during ELMs and disruptions. Starting from the initial values of Q_{IMP} and Q_{DIS}, we calculated the energy distributions during a giant ELM and disruption. The *ImpEnPlas* is the part of the escaped plasma energy deposited into the edge plasma. Comparison shows that carbon plasma is a better energy absorber of the impact energy: ∼75% of ELM energy and ∼94% of disruption energy is absorbed, compared to ∼60% and ∼89%, respectively, in the tungsten case. We calculated the percentage from the initial impact energies Q_{ELM} and Q_{DIS}. In both the C and W cases, energy absorption is more efficient during the disruption than can be explained by the stronger shielding effect. The escaped core plasma particles erode the divertor surface and form a plasma cloud from the material vapor, i.e., core plasma influences the generation of divertor plasma. In our previous study,[9] we assumed the opposite process in which generation of the divertor plasma influences the core-plasma-escaping process. Redistribution of the absorbed impact energy between the low- and high-field divertor plates (inner and outer plates) *ImpEnDiv_L* and *ImpEnDiv_H* confirms this assumption. During the ELM in both C and W cases, absorbed energy in the low-field side plate is higher than in the high-field side plate. During the disruption however, we conclude that there is opposite behavior. The high-field side plate is loaded higher than can be explained by the back-influence of the MHD processes in the divertor plasma cloud on the escaping of core plasma particles. Using carbon as the divertor plate material provides better protection of the divertor surface because the generated carbon plasma cloud absorbs and holds much of the core impact energy. However, this additional energy increases mainly the temperature of plasma cloud, while in the tungsten case it is used for additional ionization. As noted in the table, *RadEn* is the energy emitted from the entire SOL edge plasma during the ELM or disruption. In the carbon case during ELM, the divertor plasma reradiates ∼3.7% of initial energy vs. ∼45.5% in the tungsten case. The difference in divertor plasma reradiation between C and W increases with impact energy. For disruption, the reradiated energy reaches a higher value, i.e., ∼70% for the tungsten plates. However, a comparison of the radiation energies absorbed in the divertor plates during disruption (see *RadEnDiv_L* and *RadEnDiv_H* in Table I) shows less difference between the carbon and tungsten plates. This is a typical result of the divertor plate damage previously shown by the localized simulation.[6,11] Expansion of the simulation to include the entire SOL area shows fine details of the reradiated energy and spatial profile. In the W case, most of the radiation energy will be redistributed to nearby divertor components. The summary of the divertor plate evaporated mass (*EvapMassDiv_L*, *EvapMassDiv_H*) and total evaporated mass in SOL (*EvapMassTot*) is good confirmation of these predictions.

TABLE I. Summarized domain plasma parameters integrated by ELM and disruption time.[a]

	Giant ELM, $Q = 12.6$ MJ		Disruption, $Q = 126$ MJ	
Parameter (unit)	C	W	C	W
ImpEnPlas (MJ)	9.42	7.52	118.5	112.3
ImpEnDiv_L (MJ)	0.87	1.19	0.6	0.78
ImpEnDiv_H (MJ)	0.41	0.82	0.74	1.08
RadEn (MJ)	0.46	5.74	3.5	88.77
RadEnDiv_L (MJ)	0.08	0.78	0.66	3.0
RadEnDiv_H (MJ)	0.005	0.32	0.14	3.9
EvapMassDiv_L (g)	0.91	0.48	2.33	1.17
EvapMassDiv_H (g)	0.43	0.2	1.16	0.96
EvapMassTot (g)	1.51	12.2	2.72	199.4[b]

[a] *ImpEnPlas*, *ImpEnDiv_L* and *ImpEnDiv_H* is energy deposited into the SOL plasma, the low-, and high-field divertor plates, correspondingly; *RadEn* is total radiation energy derived from plasma; *RadEnDiv_L* and *RadEnDiv_L* are radiation energy deposited into the low- and high-field divertor plates; *EvapMassDiv_L* and *EvapMassDiv_H* are mass evaporated from the low- and high-field divertor plates; and *EvapMassTot* is total evaporated mass of all tokamak surfaces.

[b] Including vaporized SS components.

IV. CONCLUSIONS

We have developed multidimensional comprehensive models for extensive and integrated simulation of the evolved divertor/edge plasma during plasma instabilities and its self-consistent evolution in the entire SOL area with prediction of heat loads and erosion profiles on all nearby component surfaces. An important part of the upgraded HEIGHTS integrated package, i.e., radiation spectra with fine details and transport, is developed and presented. Based on weighted Monte Carlo algorithms, the developed radiation transport module allows full 3D simulations of radiation fluxes in the entire SOL area with detailed analysis of divertor spatial configuration (for regions of interest). Coupled with the earlier developed kinetic models of the escaping core plasma,[9] the radiation transport model was used for simulation of giant ELM and disruption in the current design of the ITER device.[29] Detailed surface thermal response due to radiation from the evolved divertor plasma was extensively modeled and analyzed. Calculation results are found to be in agreement with previous studies[6] regarding the significant increase of radiation flux and damage to divertor nearby components during disruptions. For the same core plasma impact energy, radiation flux increases with the atomic number of the divertor material. Detailed radiation spectra and comparison of the emitted radiation fluxes of carbon and tungsten as divertor plate materials are calculated and analyzed. During a disruption on the tungsten divertor plate, significant damage was predicted to the open stainless steel tubes of the dome structure in the current ITER design.

ACKNOWLEDGMENTS

This work was supported by the U.S. Department of Energy, Office of Fusion Energy Sciences.

[1] A. J. Webster, Nucl. Fusion **52**, 114023 (2012).

[2] A. V. Nedospasov, Nucl. Fusion **48**, 032002 (2008).

[3] E. J. Doyle, W. A. Houlberg, Y. Kamada, V. Mukhovatov, T. H. Osborne, A. Polevoi, G. Bateman, J. W. Connor, J. G. Cordey, T. Fujita *et al.*, Nucl. Fusion **47**, S18 (2007).

[4] V. Rozhansky, P. Molchanov, I. Veselova, S. Voskoboynikov, A. Kirk, G. Fishpool, P. Boerner, D. Reiter, and D. Coster, Plasma Phys. Controlled Fusion **55**, 035005 (2013).

[5] B. Bazylev, Yu. Igitkhanov, J. W. Coenen, V. Philipps, and Y. Ueda, Phys. Scr. T **145**, 014054 (2011).

[6] V. Sizyuk and A. Hassanein, Nucl. Fusion **50**, 115004 (2010).

[7] G. M. Staebler, Nucl. Fusion **30**, 2295 (1990).

[8] F. Ryter, S. K. Rathgeber, E. Viezzer, W. Suttrop, A. Burckhart, R. Fischer, B. Kurzan, S. Potzel, T. Pütterich, and the ASDEX Upgrade Team, Nucl. Fusion **52**, 114014 (2012).

[9] V. Sizyuk and A. Hassanein, Nucl. Fusion **53**, 073023 (2013).

[10] A. Hassanein, V. Morozov, V. Sizyuk, V. Tolkach, and B. J. Rice, "HEIGHTS-EUV package for DPP source modeling," in *EUV Sources for Lithography*, edited by V. Bakshi (SPIE, Bellingham, WA, 2006), Chap. 9, p. 277.

[11] V. Sizyuk and A. Hassanein, J. Nucl. Mater. **438**, S809 (2013).

[12] G. Miloshevsky and A. Hassanein, Nucl. Fusion **54**, 043016 (2014).

[13] A. Hassanein, V. Sizyuk, and T. Sizyuk, IEEE Trans. Plasma Sci. **39**, 2810 (2011).

[14] S. S. Harilal, T. Sizyuk, V. Sizyuk, and A. Hassanein, Appl. Phys. Lett. **96**, 111503 (2010).

[15] J. P. Apruzese, J. Davis, D. Duston, and K. G. Whitney, J. Quant. Spectrosc. Radiat. Transfer **23**, 479 (1980).

[16] B. Lipschultz, J. W. Coenen, H. S. Barnard, N. T. Howard, M. L. Reinke, D. G. Whyte, and G. M. Wright, Nucl. Fusion **52**, 123002 (2012).

[17] Ya. Zeldovich and Yu. Raizer, *Physics of Shock Waves and High-Temperature Hydrodynamics Phenomena* (Academic Press, New York, London, 1966).

[18] A. Hassanein, V. Sizyuk, V. Tolkach, V. Morozov, T. Sizyuk, B. J. Rice, and V. Bakshi, Proc. SPIE **5374**, 413 (2004).

[19] J. A. Fleck, Jr. and J. D. Cummings, J. Comput. Phys. **8**, 313 (1971).

[20] R. Siegel and J. Howell, *Thermal Radiation Heat Transfer* (Hemisphere Publishing Corporation, Washington, New York, London, 1981).

[21] V. Tolkach, V. Morozov, and A. Hassanein, "Development of comprehensive models for opacities and radiation transport for IFE systems," Argonne National Laboratory Report No. ANL-ET/02-23, Argonne, IL (2002), see http://www.ipd.anl.gov/anlpubs/2003/06/47055.pdf.

[22] S. S. Harilal, G. V. Miloshevsky, T. Sizyuk, and A. Hassanein, Phys. Plasmas **20**, 013105 (2013).

[23] F. Herman and S. Skillman, *Atomic Structure Calculations* (Prentice-Hall, Englewood Cliffs, NJ, 1963).

[24] D. Zaltzmann, *Atomic Physics in Hot Plasmas* (Oxford University Press, New York, 1998), Chap. 4.

[25] S. S. Harilal, T. Sizyuk, A. Hassanein, D. Campos, P. Hough, and V. Sizyuk, J. Appl. Phys. **109**, 063306 (2011).

[26] V. Sizyuk, A. Hassanein, V. Morozov, and T. Sizyuk, "Heights integrated model as instrument for simulation of hydrodynamic, radiation transport, and heat conduction phenomena of laser-produced plasma in EUV applications," Argonne National Laboratory Report No. ANL-MCS-CPH-06/56, Argonne, IL (2006), see http://info.mcs.anl.gov/pub/tech_reports/reports/ANL-MCS-CPH-06-56.pdf.

[27] A. Hassanein, T. Sizyuk, V. Sizyuk, and S. S. Harilal, Proc. SPIE **7969**, 79690D (2011).

[28] V. Sizyuk, A. Hassanein, and T. Sizyuk, Laser Part. Beams **25**, 143 (2007).

[29] R. Villari, V. Barabash, F. Escourbiac, L. Ferrand, T. Hirai, V. Komarov, M. Loughlin, M. Merola, F. Moro, L. Petrizzi *et al.*, Fusion Eng. Des. **88**, 2006 (2013).

[30] D. Reiter, V. Kotov, P. Börner, K. Sawada, R. K. Janev, and B. Küppers, J. Nucl. Mater. **363–365**, 649 (2007).

[31] H. A. Scott and M. L. Adams, AIP Conf. Proc. **645**, 40 (2002).

[32] T. Sizyuk and A. Hassanein, J. Appl. Phys. **114**, 083109 (2013).

[33] K. Nishihara, A. Sunahara, A. Sasaki, M. Nunami, H. Tanuma, S. Fujioka, Y. Shimada, K. Fujima, H. Furukawa, T. Kato *et al.*, Phys. Plasmas **15**, 056708 (2008).